

BNL-113937-2017-JA

Rate Dependent Multi-Mechanism Discharge of Ag0.50VOPO4·1.8H2O: Insights from in-situ Energy Dispersive X-ray Diffraction

Matthew M. Huie, David C. Bock, Zhong Zhong, Andrea M. Bruck, Jiefu Yin, Esther S. Takeuchi, Kenneth J. Takeuchi, and Amy C. Marschilok

Submitted to the Journal of the Electrochemical Society

March 2017

Energy and Photon Sciences Directorate

Brookhaven National Laboratory

U.S. Department of Energy USDOE Office of Science (SC), Basic Energy Sciences (BES) (SC-22)

Notice: This manuscript has been co-authored by employees of Brookhaven Science Associates, LLC under Contract No. DE-SC0012704 with the U.S. Department of Energy. The publisher by accepting the manuscript for publication acknowledges that the United States Government retains a non-exclusive, paid-up, irrevocable, world-wide license to publish or reproduce the published form of this manuscript, or allow others to do so, for United States Government purposes.

DISCLAIMER

This report was prepared as an account of work sponsored by an agency of the United States Government. Neither the United States Government nor any agency thereof, nor any of their employees, nor any of their contractors, subcontractors, or their employees, makes any warranty, express or implied, or assumes any legal liability or responsibility for the accuracy, completeness, or any third party's use or the results of such use of any information, apparatus, product, or process disclosed, or represents that its use would not infringe privately owned rights. Reference herein to any specific commercial product, process, or service by trade name, trademark, manufacturer, or otherwise, does not necessarily constitute or imply its endorsement, recommendation, or favoring by the United States Government or any agency thereof or its contractors or subcontractors. The views and opinions of authors expressed herein do not necessarily state or reflect those of the United States Government or any agency thereof.

Rate Dependent Multi-Mechanism Discharge of Ag_{0.50}VOPO₄·1.8H₂O: Insights from *in-situ* Energy Dispersive X-ray Diffraction

Matthew M. Huie^a, David C. Bock^b, Zhong Zhong^b, Andrea M. Bruck^c, Jiefu Yin^c, Esther S. Takeuchi^{a,b,c}*, Kenneth J. Takeuchi^{a,c}*, and Amy C. Marschilok^{a,c}*

Kenneth.takeuchi.1@stonybrook.edu, (ACM) amy.marschilok@stonybrook.edu

Ag_{0.50}VOPO₄·1.8H₂O (silver vanadium phosphate, SVOP) demonstrates a counterintuitive higher initial loaded voltage under higher discharge current. Energy dispersive X-ray diffraction (EDXRD) from synchrotron radiation was used to create tomographic profiles of cathodes at various depths of discharge for two discharge rates. SVOP displays two reduction mechanisms. reduction of a vanadium center accompanied by lithiation of the structure, or reduction-displacement of a silver cation to form silver metal. *In-situ* EDXRD provides the opportunity to observe spatially resolved changes to the parent SVOP crystal and formation of Ag⁰ during reduction. At a C/170 discharge rate V⁵⁺ reduction is the preferred initial reaction resulting in higher initial loaded voltage. At a discharge rate of C/400 reduction of Ag⁺ with formation of conductive Ag⁰ occurs earlier during discharge. Discharge rate also affects the spatial location of reduction products. The faster discharge rate initiates reduction close to the current collector with non-uniform distribution of silver metal resulting is isolated cathode areas. The slower rate develops a more homogenous distribution of reduced SVOP and silver metal. This study illuminates the roles of electronic and ionic conductivity limitations within a cathode at the mesoscale and how they impact the course of reduction processes and loaded voltage.

Introduction

Polyanion-type materials such as LiFePO₄ have been heavily researched as battery cathodes because of their impressive stability and high operating voltage relative to oxide based materials (1-3). The thermal stability of the polyanion framework improves battery safety especially under demanding conditions. Furthermore, chemical stability of the polyanion can reduce cathode dissolution relative to oxides, extending the battery's lifetime. Specifically, for battery systems used to power implantable cardioverter defibrillators (ICD), silver vanadium phosphate (Ag_wV_xP_yO_z, SVOP) materials have been shown to minimize cathode dissolution compared to the commercially utilized silver vanadium oxide cathode (4-6), creating the potential for improved ICD batteries with extended longevity (7-15). However, a significant limitation of phosphate-based

^aDepartment of Materials Science and Engineering, Stony Brook University, Stony Brook, NY 11794, USA

^bEnergy Sciences Directorate, Brookhaven National Laboratory, Upton, NY 11973, USA ^cDepartment of Chemistry, Stony Brook University, Stony Brook, NY 11794, USA

^{*}corresponding authors: (EST) esther.takeuchi@stonybrook.edu, (KJT)

cathodes is their inherently poor electrical conductivity. Silver vanadium phosphates are able to overcome this issue due to the incorporation of silver. As SVOP compounds are reduced, silver is reduced *in-situ*, forming a conductive network of silver nanoparticles that can improve electrical conductivity by $\sim 15,000$ fold (14).

In-situ energy dispersive X-ray spectroscopy (EDXRD) is a powerful technique that can be used to better understand the mechanisms of electrochemical discharge in SVOP materials. EDXRD utilizes white, collimated X-rays as the incident beam, which is scattered by the sample (16). The resulting diffraction patterns are distributed in the selected energy range and captured by a detector held at a fixed angle. The light source is synchrotron based in order to emit the high-energy radiation needed to penetrate high density materials, including steel. The fixed diffraction angle geometry and high flux make synchrotron based EDXRD a powerful tool for in-situ study of fully sealed systems.

The features of EDXRD make it especially applicable for *in-situ* research of batteries. Results indicate that the tomographic feature of EDXRD can provide material status information as a function of location, which significantly strengthens the understanding of the cathode reduction mechanism. An early example is study of sodium/halide cells, where EDXRD was applied to track the phase change upon charging where NaCl, M (M=Ni and/or Fe), MCl₂ and Na₆FeC₁₈ were detected (17). LiMn₂O₄ cathodes in coin cell Li-ion batteries have been investigated using EDXRD, which elucidated the expansion and contraction of cathode crystal lattice parameters during discharge and charge (18). EDXRD was also used in a phase study of FePO₄ and LiFePO₄ which demonstrated asynchronous discharge (19-21) and to probe commercial alkaline batteries to monitor zinc oxide and manganese oxide phase changes (22-24). A similar synchrotron based technique to EDXRD called energy scanning confocal XRD (ES-XRD) has been described, where the incident beam and detector beam remain at fixed angles, yielding Bragg reflections from a confocal point optically defined by collimating slits (25). ES-XRD offers the advantage of improved peak resolution compared to EDXRD, and has been used to elucidate the factors limiting the capacity of highly dense electrodes composite electrodes comprised of LiNi_{1/3}Co_{1/3}Mn_{1/3}O₂(NCM) active materials, conductive additives and binders (26).

Previous EDXRD measurements of the Ag_wV_xP_vO_z family of cathode materials focused on the materials Ag₂VO₂PO₄ (27) and Ag₂VP₂O₈ (28-30). Both materials form silver metal as an initial reduction product, providing an electrically conductive matrix throughout the cathode. *In-situ* EDXRD of Ag₂VO₂PO₄ revealed the spatial distribution of silver metal during the reduction process of a cathode with no conductive additives (i.e. carbon). Silver formed initially at the electrode-electrolyte interface and propagated throughout the cathode as discharge continued. In-situ EDXRD studies of pure Ag₂VP₂O₈ indicated silver metal formation at the current collector and the anode-facing surface of the cathode but little silver formation in the center during the initial stages of discharge (29). Without conductive additives and at a slower rate of discharge, the reduction of Ag⁺ to Ag⁰ was preferred to the reduction of V⁴⁺ to V³⁺ and a slower rate of discharge resulted in a more even spatial distribution of silver metal than a faster rate (28). In-situ EDXRD was also used to study the effect of conductive additives with Ag₂VP₂O₈ (30). When carbon (15 wt%) was mixed into the cathode the dependence of silver formation with rate of discharge was different than cathodes without conductive additives. Cathodes with Ag₂VP₂O₈ and carbon produced smaller and more evenly distributed silver metal particles when discharged at faster rates. discharge resulted in the formation of larger silver particles with less total surface area that were less effective in electrically connecting active material particles, causing a lower achieved capacity.

The results reported here use *in-situ* EDXRD with spatial resolution to investigate the reduction of Ag_{0.50}VOPO₄·1.8H₂O cathodes for the first time to probe the counterintuitive higher initial loaded voltage seen under higher current discharge. Previous publications on the initial reduction mechanism for Ag_{0.50}VOPO₄·1.8H₂O report an initial high voltage plateau and indicate the preferred reduction of V⁵⁺ to V⁴⁺, which is then followed by the reduction of Ag⁺ to Ag⁰ (7, 10, 12). In this study, Li/Ag_{0.50}VOPO₄·1.8H₂O cells were discharged at two rates, faster and slower, to further probe the reduction mechanism. *In-situ* EDXRD combined with electrochemical impedance spectroscopy measurements indicated that the initial reduction process of Ag⁺ or Vⁿ⁺ cations is rate dependent and demonstrates spatial variation within the cathode, providing mechanistic insight into the bimetallic reduction process.

Experimental

Material Synthesis and Characterization

 $Ag_{0.50}VOPO_4\cdot 1.8H_2O$ (referred to as SVOP) was synthesized hydrothermally for 24 hours at 180 °C in Teflon-lined autoclaves using a method adapted from previous reports (7, 12). Reactants included stoichiometric amounts of silver powder (Alfa Aesar), V_2O_5 (GfE metalle und materiallien), phosphoric acid (BDH) and deionized water. The crystal structure of SVOP was determined by powder x-ray diffraction using a Rigaku Miniflex x-ray diffractometer with a Cu K α source. Elemental ratios were confirmed by inductively coupled plasma optical emission spectroscopy (ICP-OES) using a Thermo Scientific iCAP 6000 series ICP spectrometer. Water content was measured by thermogravimetric analysis (TGA) with a TA Instruments SDT Q600.

Electrochemical Testing

Cathode pellets, 13 mm diameter and ~0.42 mm thick, were prepared by mixing 95 wt% SVOP with 5 wt% graphite (Fisher Scientific) powders in a SPEX 8000M Mixer/Mill and pressing for 60 seconds. Stainless steel coin cells were constructed with cathode pellets, Celgard 2500 separators, Li metal anodes and an electrolyte of 1 M LiBF₄ in propylene carbonate (PC)/ dimethyl carbonate (DMC) (50/50 by volume). Coin cells were discharged at different rates using a Maccor battery tester. One group of cells was discharged at a slower rate of 0.27 mA per gram of active material (C/400) and the other group was discharged at a faster rate of 0.64 mA/g (C/170). Within each group, cells were discharged to 0.1, 0.2, 0.4, 0.6 and 1.0 electron equivalents. Electrochemical impedance spectroscopy (EIS) was performed on coin cells before and after discharge using a Biologic multi-channel potentiostat in the frequency range between 1 mHz and 1 MHz at 30 °C.

In-situ energy dispersive x-ray diffraction (EDXRD) was performed at beamline 6-BM of the Advanced Photon Source (APS) at Argonne National Laboratory (ANL). Coin cells were intact and discharged prior to the EDXRD analysis. White beam X-ray radiation (~50-200 keV) was narrowed to a beam height of 20 microns using receiving slits. The parameters of the gauge volume of the beam inside the coin cell were 3 mm width, 4 mm length and 20 micron height. Coin cells were placed on a programmable motorized stage that positioned the cell so that EDXRD patterns could be measured as a

function of position in the cathode. Coin cells were positioned such that the beam gauge volume probed the center point of the coin cell. Scans were conducted by sweeping an energy range while the detector was configured such that $2\theta=3.0^{\circ}$. A more detailed description of the experimental setup has been previously reported (24, 27, 29).

After the EDXRD measurement, cells were disassembled for *ex-situ* analysis. Coin cells were disassembled and cathode pellets were recovered, washed with dimethyl carbonate and dried. Pellets were then ground prior to powder XRD using a Rigaku Miniflex x-ray diffractometer with a Cu $K\alpha$ source.

Results

Material Characterization

The crystal structure of the synthesized SVOP material was determined with powder XRD. SVOP crystal structure was indexed with the triclinic space group $P\overline{1}$ and matched previously reported powder diffraction pattern PDF#: 97-016-2386 (31). Elemental composition of synthesized SVOP material was determined from ICP-OES and crystalline lattice water content was calculated from mass loss during heating to 580° C during TGA. The final chemical formula was determined to be $Ag_{0.50}VOPO_4\cdot 1.8H_2O$.

Electrochemical Results

Cells were discharged at rates of C/400 and C/170 to 0.1, 0.2, 0.4, 0.6 and 1.0 electron equivalents, where one electron equivalent corresponds to the insertion of one mole of lithium per mole of SVOP. Discharge curves presented as voltage versus capacity for the two rates are shown in Figure 1. Surprisingly, cells discharged at C/170 operated a higher voltage than the cells discharged at C/400 during the first 0.2 electron equivalents. After 0.2 electrons the cells with the faster C/170 rate operating at lower voltages than cells discharged at the slower C/400 rate.

Electrochemical impedance spectroscopy (EIS) was performed at each depth of discharge (DOD) level. Nyquist plots of the spectra and the R_{ct} values are plotted in Figure 1 with their corresponding DOD indicated on the discharge curve. Results from EIS were fit using the equivalent circuit model in Supplemental Information Figure S1 and select fitting results are presented in Supplemental Information Table S1. For cells discharged at either rate, R_{ct} values initially increase during the first 0.1 electrons discharge (Figure 1a) and then decrease during the later stages of discharge.

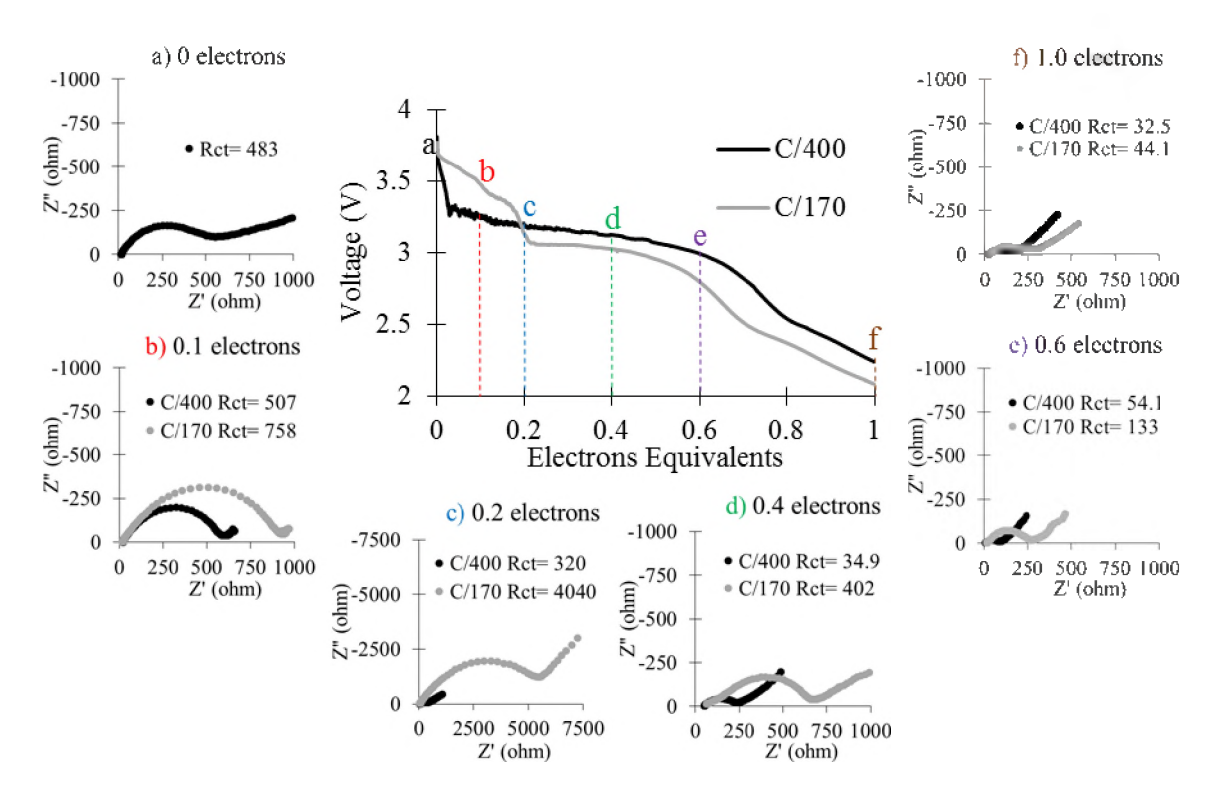


Figure 1. Discharge curves shown as voltage versus capacity in electron equivalents. Nyquist plots of the electrochemical impedance spectra (EIS) at a) 0, b) 0.1, c) 0.2, d) 0.4, e) 0.6, and f) 1.0 electron equivalents depth of discharge (DOD) are also provided. The charge transfer resistance (R_{ct}) at each point of DOD is given in each Nyquist plot. R_{ct} was determined from fitting the EIS data with the model in the Supplemental Information Figure S1.

Interestingly, a decrease in charge-transfer resistance occurs at slightly different DODs for the two discharge rates tested in this report. The R_{CT} is plotted versus discharge for the two rates and shown in Figure S2. The cells discharged more slowly (C/400) increase in charge-transfer resistance from 483 ohms (Figure 1a) to 507 ohms (Figure 1b) during the first 0.1 electron of discharge and then decrease in charge-transfer resistance to 320 ohms (Figure 1c) at 0.2 electron DOD and beyond. The faster discharged cells (C/170) showed significant increases in charge-transfer resistance to 0.2 electron DOD with a maximum resistance of 4,040 ohms at 0.2 electrons DOD (Figure 1c) and then subsequent decreases beyond 0.2 electron DOD.

In-situ EDXRD

In-situ EDXRD was used to probe the effect of discharge rate on the reduction mechanism of Ag_{0.50}VOPO₄·1.8H₂O. The technique enabled *in-situ* visualization of cathode lithiation and spatial distribution of metallic silver formation by measuring a tomographic diffraction profile of the intact coin cells. Tomographic profiles were collected in the center (x, y position) of the cell while the height (z) of the cathode was moved in increments of 20 μm. Scans accumulated diffraction intensity as a function of beam energy. Energy was converted to inverse d-spacing with the measurement of a lanthanum hexaboride (LaB₆) calibration standard. Plots of *in-situ* EDXRD profiles for the non-discharged cell and cells discharged to 0.6 and 1.0 electrons DOD are shown in

Figure 2. Plots at 0.1, 0.2 and 0.4 electrons for both rates are given in the Supplemental Information (Figure S3). A height of 0 microns represents the side of the cathode adjacent to the stainless steel current collector. Each scan increases in height in increments of 20 microns. The three peaks chosen for *in-situ* EDXRD analysis and indicated on Figure 2 were at d⁻¹ values of 0.393, 0.425 and 0.461 Å⁻¹. The peak at 0.425 Å⁻¹ represents the (111) plane from formation of metallic silver during the reduction of Ag⁺ to Ag⁰. The peak at 0.461 Å⁻¹ indicates the (006) plane of the initial phase of SVOP which decreases in intensity during discharge. The peak at 0.393 Å⁻¹ is not apparent in the initial SVOP structure then begins to form at 0.4 electrons DOD and will be referred to as the "reduced phase". Notably, cells discharged at C/400 show a more uniform intensity throughout the cathode while cells discharged at C/170 display an uneven distribution of peak intensity with more intense peaks on the side of the cathode facing the lithium anode.

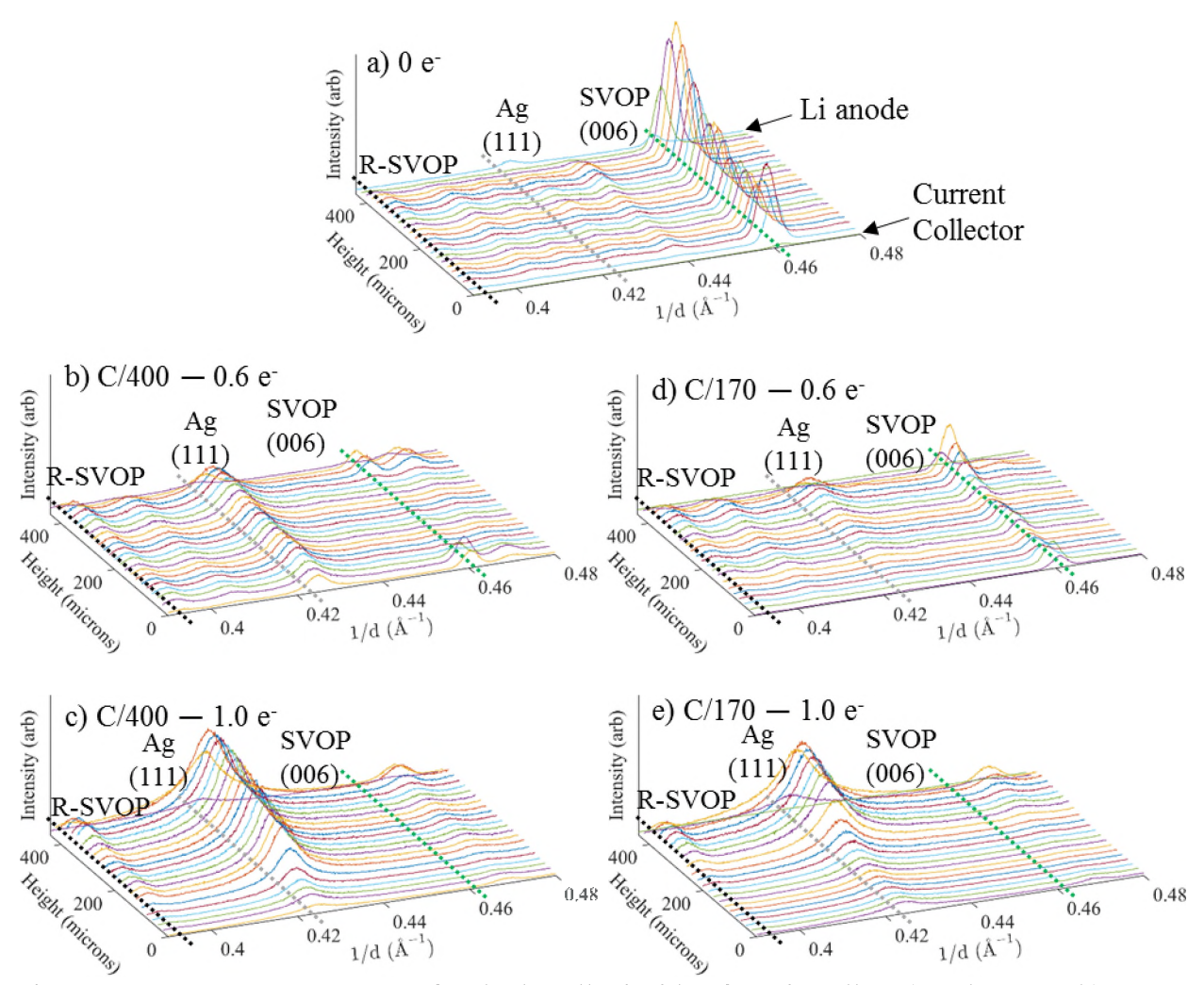


Figure 2. *In-situ* EDXRD scans of cathode pellet inside of a coin cell at a) 0 electrons, b) 0.6 electrons at C/400, c) 1.0 electrons at C/400 (bottom left), d) 0.6 electrons at C/170, e) 1.0 electrons at C/170. Height of 0 microns indicates the side of the pellet facing the stainless steel casing. Dotted lines indicate the reduced SVOP phase at 0.393 Å⁻¹ (black), Ag peak at 0.425 Å⁻¹ (gray), and initial SVOP phase at 0.461 Å⁻¹ (green).

In Figure 3 the *in-situ* EDXRD silver peak was plotted at three positions within the cathode to highlight the differences in intensity with cathode position between the two discharge conditions. Figure 3a and 3d show cathode positions adjacent to the stainless steel current collector, Figure 3b and 3e show positions in the middle of the cathode, and Figure 3c and 3f show cathode positions facing the lithium anode. Cells discharged at both discharge rates demonstrate similar diffraction patterns at the lithiumfacing side with peaks corresponding to Ag⁰ present by 0.6 electrons DOD and initial SVOP peaks decreasing in intensity until no longer apparent at 1.0 electrons DOD. However, there are stark differences between the two rates for diffraction patterns collected in the center and current collector-facing positions of the cathode. For the C/400 cells, diffraction patterns collected at the center position (Figure 3b) progress similarly to the lithium-facing side of the cathode (Figure 3c). Diffraction patterns collected at the center position (Figure 3e) of the C/170 cells are approximately half as intense as of the diffraction patterns from the C/400 cells (Figure 3b) for both SVOP and Ag peaks. Thus, the C/170 discharge rate causes comparably more SVOP crystal structure change in the center position while reducing less Ag^+ to Ag^0 . At the interface of the cathode and current collector the differences are more pronounced. Near the current collector cells discharged at C/170 (Figure 3d) show little crystallinity from 0.1 electron DOD to 0.6 electron DOD while cells discharged at C/400 (Figure 3a) retained some crystallinity near the current collector throughout discharge. There is an observable metallic silver peak in this position at 1.0 electron DOD, but it is significantly less intense than the same position in the cells discharged at C/400. Silver formation occurs more homogeneously at earlier DODs for cells discharged at the C/400 rate, resulting in lower impedances at early DOD. Also, cells discharged at C/400 maintain the intensity of SVOP peaks near the current collector throughout the first stages of reduction. indicates that the SVOP material discharged at C/170 becomes amorphous at earlier DOD (0.2 electrons) compared with the cells discharged at C/400 (0.6 electrons).

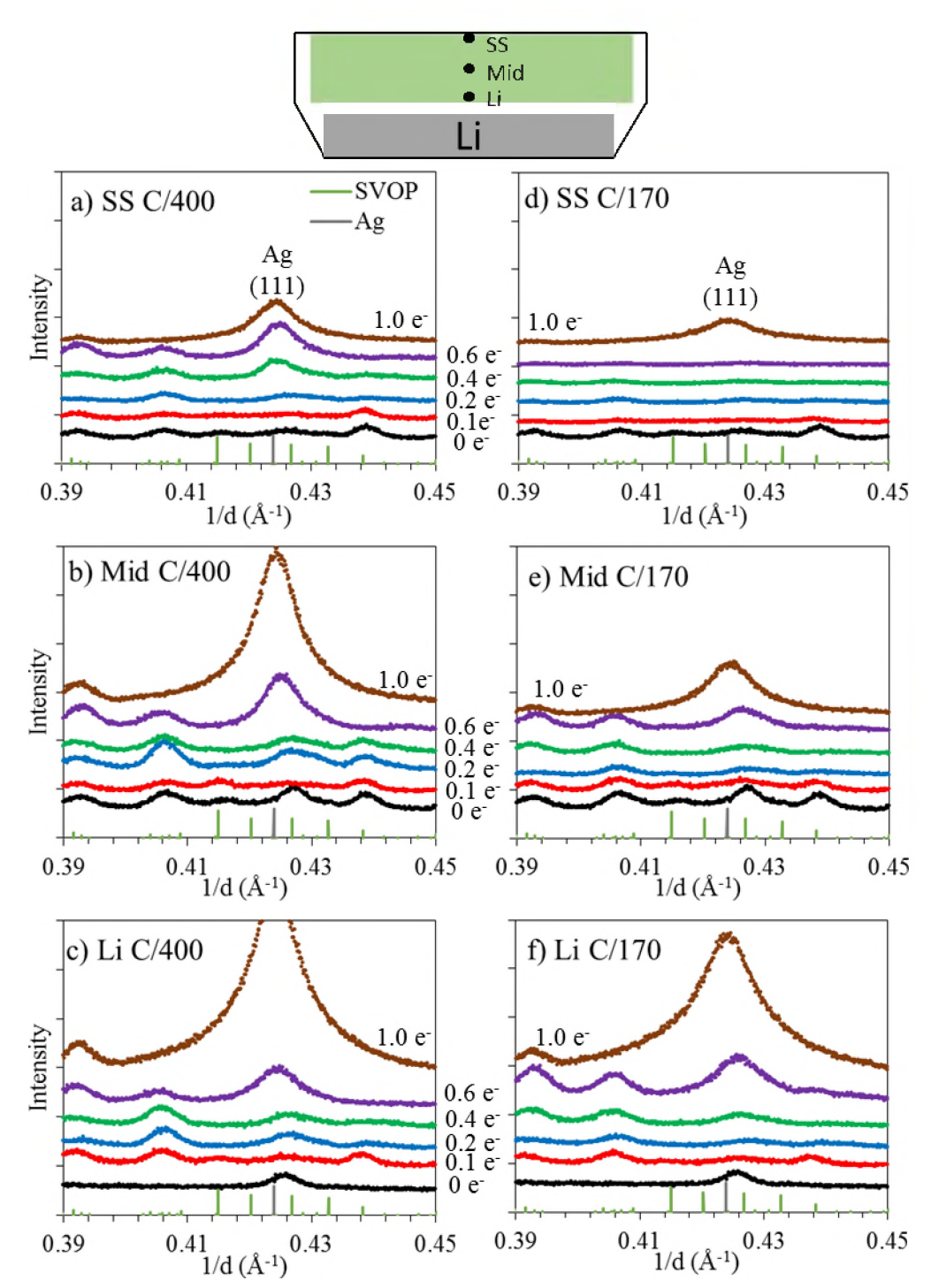


Figure 3. Formation of the silver peak as a function of discharge at different locations within the cathode pellet. Top schematic shows basic representation of coin cell with three positions indicated. Discharge rate of C/400 is shown in a, b, and c and the discharge rate of C/170 are shown in d, e and f. Scans of the side of the pellet facing the stainless steel (SS) current collector are shown in a and d. Scans of the middle (Mid) of the pellet are shown in b and e. Scans of the side of the pellet facing the lithium (Li) anode are shown in c and f. 0 electrons DOD patterns are black, 0.1 electrons DOD patterns are red, 0.2 electrons DOD patterns are blue, 0.4 electrons DOD are green, 0.6 electrons DOD patterns purple and 1.0 electrons DOD patterns are brown. Green lines at

the bottom of the figure indicate reflections of the SVOP parent phase and the grey line represents the (111) reflection of the Ag^0 phase.

Progression of the maximum peak intensities of peaks with d⁻¹ spacings of 0.425, 0.461, and 0.393 Å⁻¹ throughout the entire cathode are depicted in Figure 4, 5, and 6, respectively. Notably there are non-uniform intensities of the non-discharged cell observed. The likely cause for uneven peak intensities for the non-discharged cell is variation in x-ray attenuation from the cathode pellet or stainless steel casing throughout the height of the cell. There may also be some preferential orientation of cathode particles as SVOP material forms plate-like structures that have shown preferential alignment during packing in previous powder XRD (12).

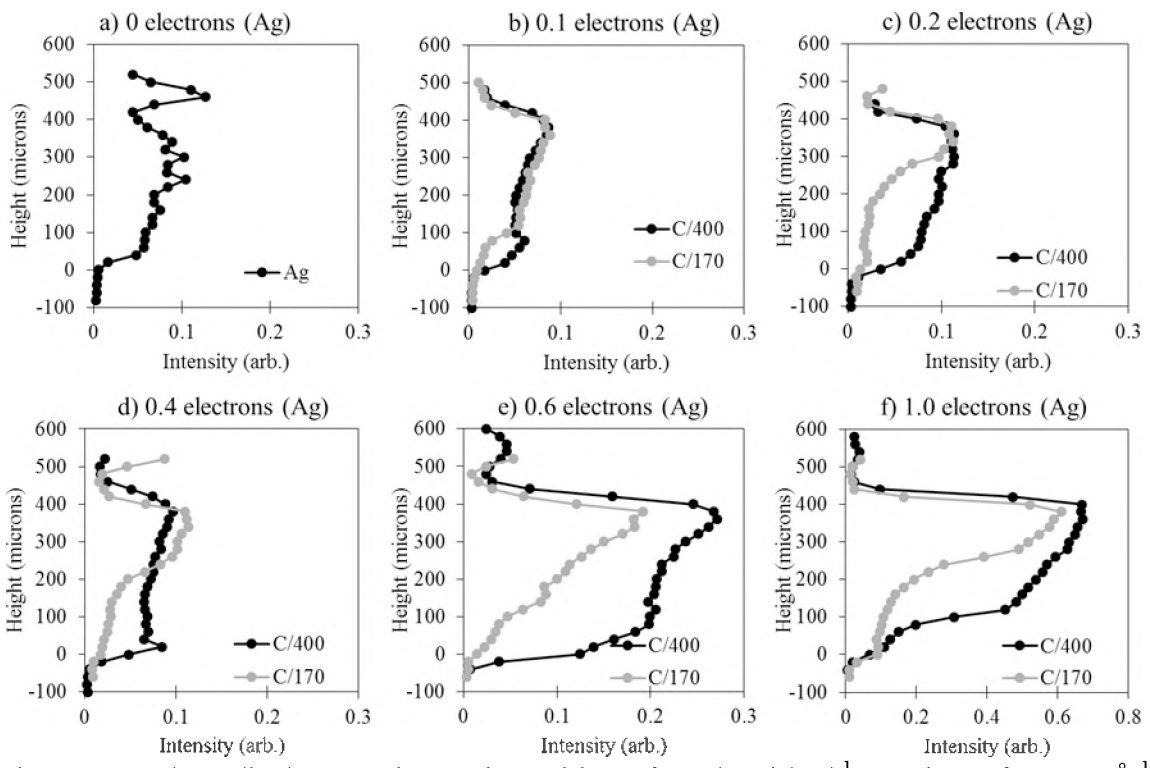


Figure 4. Plots display maximum intensities of peak with d^{-1} spacing of 0.425 Å⁻¹ corresponding to the (111) plane of metallic silver. Each plot represents a point along the discharge curve in terms of electron equivalents depth of discharge a) 0 electrons, b) 0.1 electrons, c) 0.2 electrons, d) 0.4 electrons, e) 0.6 electrons and f) 1.0 electrons. Note the change in scale of x-axis value for the plot of 1.0 electrons. A height of 0 microns correlates to the interface of the stainless steel current collector and the $Ag_{0.50}VOPO_4\cdot 1.8H_2O$ (SVOP) pellet. Cathodes were ~420 microns thick.

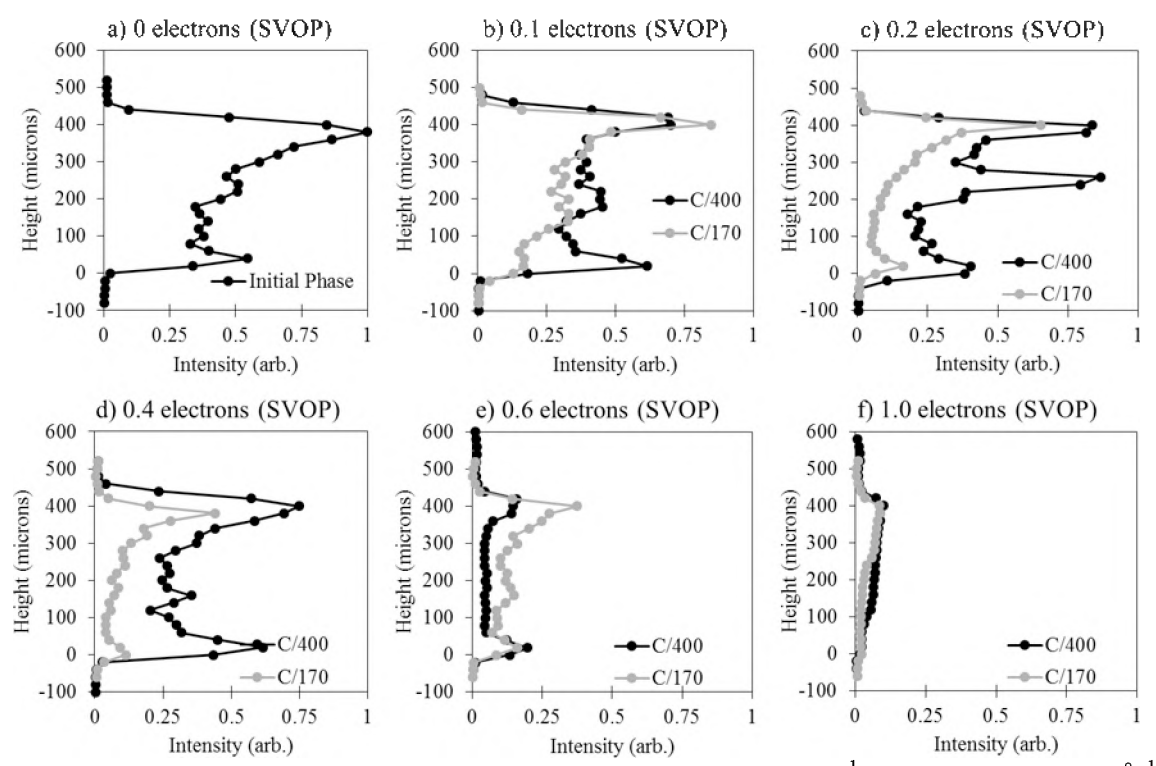


Figure 5. Plots display maximum intensities of peak with d^{-1} spacing of 0.461 Å⁻¹ corresponding to the (006) plane of SVOP. Each plot represents a point along the discharge curve in terms of electron equivalents depth of discharge a) 0 electrons, b) 0.1 electrons, c) 0.2 electrons, d) 0.4 electrons, e) 0.6 electrons and f) 1.0 electrons. A height of 0 microns correlates to the interface of the stainless steel current collector and the $Ag_{0.50}VOPO_4\cdot 1.8H_2O$ (SVOP) pellet. Cathodes were ~420 microns thick.

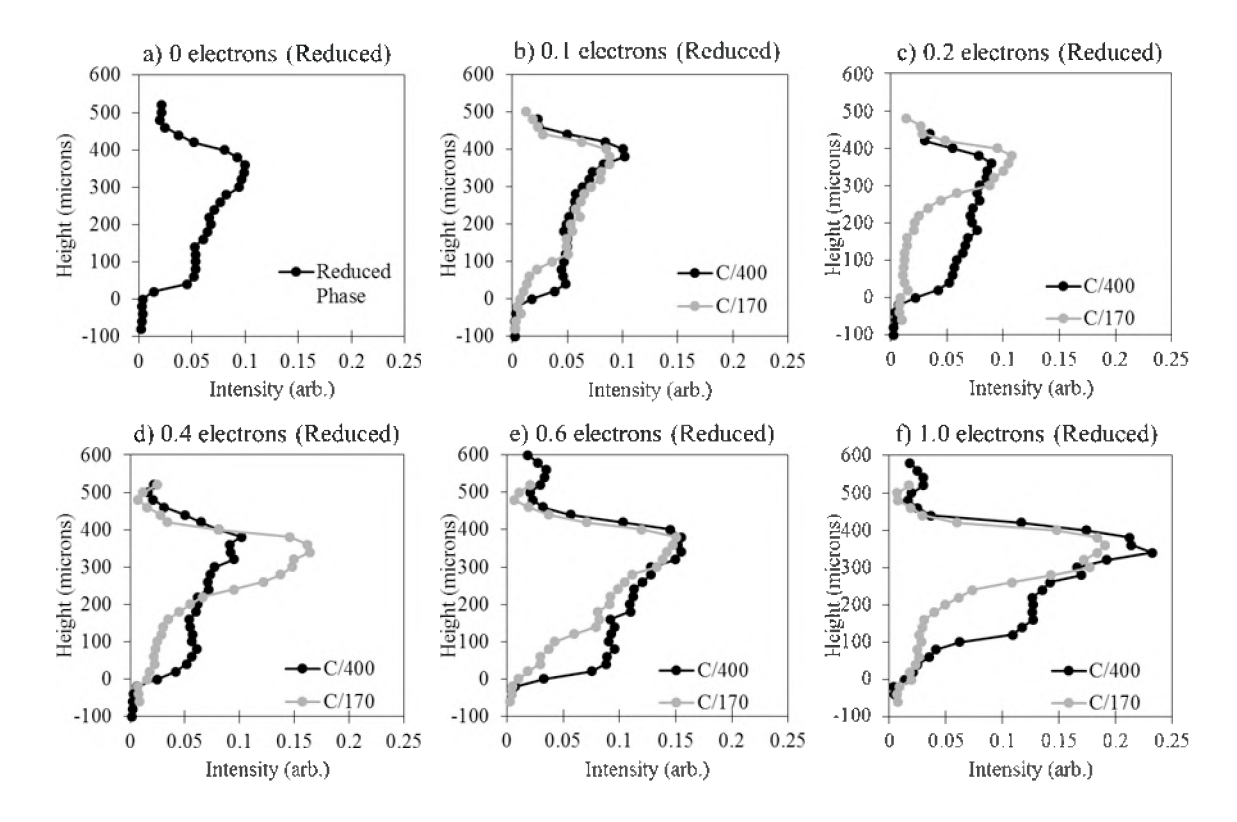


Figure 6. Plots display maximum intensities of peak with d^{-1} spacing of 0.393 Å⁻¹ corresponding to the reduced phase formed during SVOP lithiation. Each plot represents a point along the discharge curve in terms of electron equivalents depth of discharge a) 0 electrons, b) 0.1 electrons, c) 0.2 electrons, d) 0.4 electrons, e) 0.6 electrons and f) 1.0 electrons. A height of 0 microns correlates to the interface of the stainless steel current collector and the $Ag_{0.50}VOPO_4\cdot 1.8H_2O$ (SVOP) pellet. Cathodes were ~420 microns thick.

 $\mathit{In\text{-}situ}$ EDXRD indicated that discharge rate affects the location of Ag^0 nucleation and subsequent formation of a conductive metal network. The onset of metallic silver formation is not clearly identifiable at 0.1 electron DOD as the diffraction intensities in Figure 5 show minimal differences between the intensities of the nondischarged cell (Figure 5a) and those discharged to 0.1 electrons (Figure 5b). The lack of Ag⁰ diffraction intensity at 0.1 electron DOD agrees with the charge transfer resistances calculated from AC impedance (Figure 1) which increased during the first 0.1 electrons of discharge insinuating that there is no conductive metal network by 0.1 electron DOD. At 0.2 electron DOD (Figure 5c) Ag⁰ formation becomes apparent but with different distributions for each discharge rate. The formation of metallic silver is more homogenous throughout the cathode at 0.2 electron for cells discharged at C/400 while the anode-facing side of the cathode is more preferred for Ag⁰ nucleation at C/170 (Figure 5c). Further Ag^+ reduction occurs close to the already formed Ag^0 nanoparticles so the propagation of the Ag^0 network appears to stem from Ag^0 nucleation sites. At 0.6 (Figure 5e) and 1.0 electron (Figure 5f) DOD the C/170 rate displayed more intense silver diffraction near the anode-facing side while the cells discharged at C/400 showed more uniform silver metal through the thickness of the cathode. This trend of homogeneity (C/400) and heterogeneity (C/170) for the two discharge rates is also seen in the increase in peak intensity of the reduced phase peak at 0.393 Å⁻¹. Regression of the parent SVOP phase peak intensity also followed a homogeneous (C/400) versus heterogeneous (C/170) pathway. For the C/170 discharge rate SVOP peak intensity near the current collector drops off significantly by 0.1 electron DOD (Figure 6b) and becomes almost indistinguishable from background intensity by 0.2 electron DOD (Figure 6c). Cells discharged at C/400 do not exhibit this behavior as they display SVOP peak intensity at 0.461 Å⁻¹ through the entire cathode up to 0.4 electron DOD (Figure 6d). The loss of SVOP diffraction intensity could indicate vanadium reduction as the loss of SVOP intensity is not correlated with an increase in Ag⁰ intensity. For example at 0.4 electrons DOD the C/170 rate displayed low intensities of SVOP and Ag⁰ peaks near the current collector so the parent SVOP phase had been changed but without much Ag^0 formation. Li⁺ insertion without Ag^+ displacement out of the crystal structure could cause amorphization of the parent phase and reduction of vanadium. There is less SVOP intensity at earlier DODs in the C/170 cells which indicates a greater level of vanadium reduction. Based on *in-situ* EDXRD, discharge rate dictated the preference of V^{5+} or Ag^{+} reduction as well as the spatial distribution of Ag^{0} nucleation sites and resulting Ag^{0} network formation.

Ex-situ XRD

After the EDXRD measurement, cells were disassembled for *ex-situ* XRD analysis, Figure 7. Data are plotted with a 2θ axis corresponding to a copper radiation source. For reference, inverse d-spacing of 0.393, 0.425, and 0.461 Å⁻¹ equate to

approximately 35.2, 38.2 and 41.5° in Cu 2θ , respectively. Supplemental Information Figure S5 shows the non-discharged cathode closely matches the reported triclinic pattern for $Ag_{0.43}VOPO_4\cdot 2H_2O$ (PDF#: 97-016-2386) (31) and Figure S6 compares the ex-situ XRD data at the two discharge rates. Diffraction patterns of cathodes discharged to higher DODs decrease in intensity of (004) and (006) reflections of the SVOP phase, occurring simultaneous to an increase in intensity of Ag^0 peaks. The inset in Figure 7 shows the (002) reflection of SVOP is retained and shifts during discharge. This shift towards a higher 2θ angle indicates a decrease in lattice spacing of the (002) planes consistent with the removal of Ag^+ from between these layers and replacement with a smaller Li^+ ion (10). Displacement of Ag^+ during reduction leads to the collapse of the (004) and (006) reflections and formation of lithiated VOPO₄ layered structure with an (002) reflection.

Overall, *ex-situ* diffraction patterns for cathodes discharged at the two rates are similar as a function of discharge, with the Ag^0 (111) peak clearly forming at $2\theta = 38.2^{\circ}$ by 0.6 electron equivalents and increasing in intensity by 1.0 electron equivalent. While the initial SVOP peaks drop in intensity for both rates during reduction, the cathodes discharged at C/170 show a decrease in SVOP peak intensity at earlier DODs relative to cathodes discharged at C/400 (Supplemental Information Figure S4). For example, the peak near 41.5° SVOP (006) fades with increasing DOD. This peak is still noticeable at 0.4 electrons when discharged at C/400 but is not as distinguishable at 0.4 electrons when discharged at C/170, providing further evidence that the faster C/170 discharge rate provokes a breakdown in the parent SVOP structure. Formation of a new "reduced" or lithiated phase can be observed at 0.4 electrons DOD characterized by a peak at 35.2° with retention of some peaks between 27-30°.

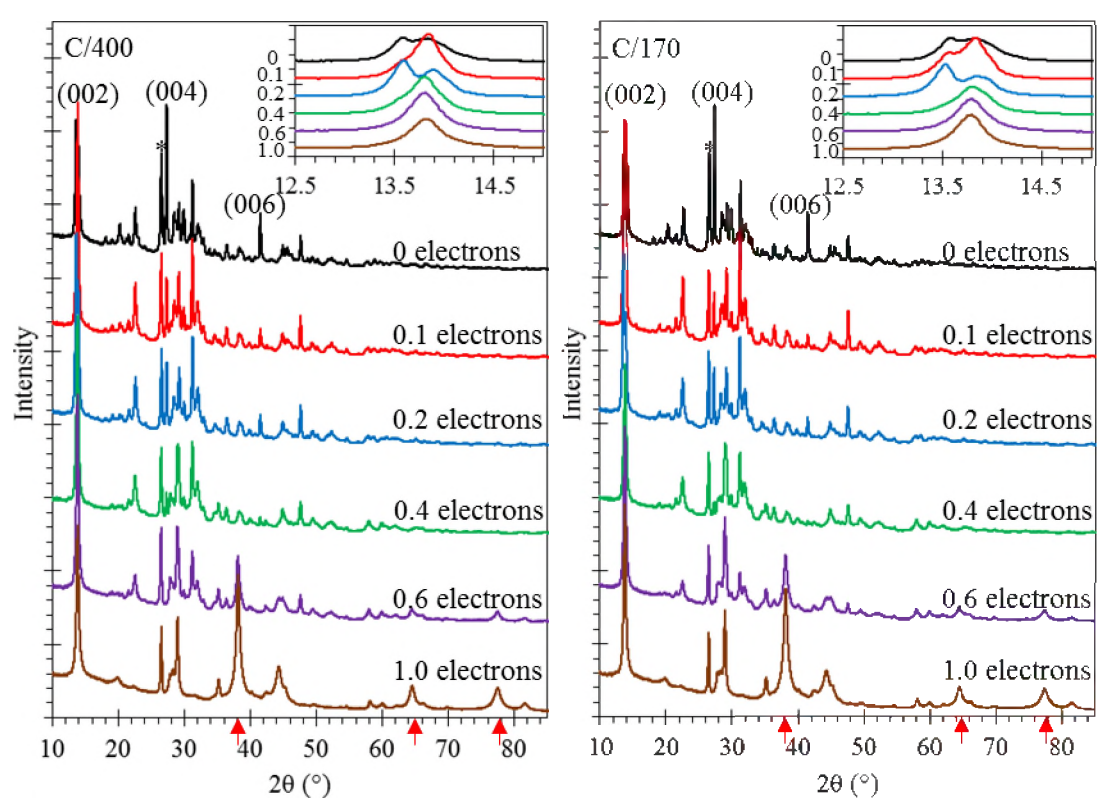


Figure 7. *Ex-situ* XRD patterns between 2θ values of 10-85 degrees for cathodes at different depths of discharge (DOD) and rates of C/400 (left) and C/170 (right). Peaks at

2θ values of 35.2, 38.2, and 41.5 degrees correspond to d⁻¹ spacings of 0.393 Å⁻¹, 0.425 Å⁻¹ 0.461 Å⁻¹, respectively, which were chosen to analyze with EDXRD. The graphite peak near 26.5° is labeled with an asterisk (*). The (002), (004) and (006) planes of the parent SVOP phase are marked. Red arrows on the x-axis represent peak positions of metallic Ag⁰. Inset figures show a magnified view of the evolution of the (002) peak during discharge.

Discussion

Rate-Dependent Reduction Mechanism

Previous reports separated the reduction of SVOP into two stages: 1) preferred V^{5+} reduction to V^{4+} with a small amount Ag^0 formation during the first 0.5 electrons DOD and 2) concomitant reduction of vanadium and Ag^+ at DODs beyond 0.5 electrons(10, 12, 32). During the first stage there is Li^+ insertion but minimal Ag^+ displacement and subsequent Ag^0 formation, and as such the SVOP cathode remains fairly resistive. After most of the V^{5+} is reduced by 0.5 electrons DOD, the amount of Ag^0 rapidly increases and cathode resistivity sharply drops. None of the previous publications explored the relationship of discharge rate to the reduction mechanism. This *in-situ* EDXRD study investigates how discharge rate affects the proportions of V^{5+} reduction to Ag^+ reduction during the first stage of discharge, impacting the voltage and resistance of the cell as well as the reduction mechanism at later DODs.

In order for V^{5+} to reduce to V^{4+} there must be Li^+ insertion into the SVOP parent structure to balance charge. In contrast, Ag^+ reduction occurs by Ag^+ migration from its position between layers of corner sharing VO_5 and PO_4 and replacement with Li^+ , with Ag^0 forming on surface of the SVOP particle. Thus, while V^{5+} reduction incorporates both Li^+ and Ag^+ ions into the SVOP parent structure, Ag^+ reduction results in replacement of Ag^+ with a smaller Li^+ ion. It can be reasonable that the inclusion of two cations in the SVOP layers during V^{5+} reduction causes distortion of the crystal structure, resulting in loss of diffraction intensity from the SVOP phase. In contrast, the reduction of Ag^+ does not cause as severe of a change to the crystal structure because there is no net difference in the amount of cations between layers. This hypothesis coincides well with the observations from *in-situ* EDXRD and electrochemical tests.

In-situ EDXRD indicates that the C/170 rate promotes amorphization of the SVOP crystal structure during the first 0.2 electrons of reduction (Figure 5c). At 0.2 electrons DOD cells discharged at C/170 exhibited SVOP peak intensity comparable to the nondischarged cell for the anode-facing side of the cathode, but SVOP peak intensity decreases considerably as the scan position moves closer to the current collector until SVOP peak intensity is almost indistinguishable from background noise. Peak intensities of SVOP did not follow this trend for cells discharged at C/400. Thus, if V^{5+} reduction does cause amorphization due to distortion of SVOP crystal structure, then the EDXRD data suggests V⁵⁺ is heavily preferred at a C/170 rate. At faster rates of discharge with higher flux of electrons, the reduction mechanism will prefer the more facile pathway for ion transport. Li⁺ insertion into the parent structure to reduce V⁵⁺ may be more kinetically favorable than the ionic transport of larger Ag⁺ ions out of the structure to reduce on the particle surface because Li⁺ ions are much smaller and contain less mass than Ag⁺ ions. Based on size and mass, smaller and lighter ions would be expected to have greater mobility and as such V⁵⁺ reduction would be preferred at the faster rate. In contrast, at C/400, the minimal loss of SVPO diffraction intensity indicates that Ag

reduction accompanies V^{5+} reduction during the first stage of discharge, indicating the kinetics of Ag^+ migration can be accommodated at the slower rate.

Electrochemical results also support the finding that the C/170 discharge rate results in preferential V⁵⁺ reduction and the C/400 rate evokes preferential Ag⁺ reduction during the first stage of discharge. V⁵⁺ has a more positive standard reduction potential than Ag⁺, and as such V⁵⁺ is expected to have a higher operating voltage in a Li-ion battery than Ag⁺ (33). In Figure 1 the C/170 discharge rate produced a higher voltage during the first 0.2 electrons DOD than the C/400 rate, suggesting that cells discharged at C/170 undergo V⁵⁺ reduction during this early stage of discharge instead of Ag⁺ reduction. Furthermore, the EIS data depicted in Figure 1 show that charge transfer resistance of cells discharged at C/170 increases through 0.2 electrons DOD (R_{ct}=4,040 ohms) while cells discharged at C/400 decrease in charge transfer resistance between 0.1 (R_{ct}=507 ohms) and 0.2 electrons DOD (R_{ct}=320 ohms). EIS data suggests cathode conductivity improves during the early stages of reduction at a C/400 rate because Ag⁰ is formed. However, at C/170 V⁵⁺ reduction is preferred and charge transfer resistance increases significantly. In other silver vanadium phosphorous oxide cathodes with different stoichiometry, such as Ag₂VO₂PO₄ (7, 11, 12, 15, 30, 34) and Ag₂VP₂O₈ (9, 13, 29, 30), an initial decrease in the charge transfer resistance coincides with the reduction of Ag⁺ to form conductive metallic silver. An increase in charge transfer resistance associated with V⁵⁺ reduction is reminiscent of the 5x increase in charge transfer resistance during the reduction of ε -VOPO₄ (35). By analogy, the study is relevant to the lithiation of SVOP because SVOP retains the VOPO₄ sublattice structure during lithiation, and as such the reduced phase of SVOP may behave similarly to lithiated ε-There are also studies showing substantial increases in charge transfer resistance of $\text{Li}_3\text{V}_2(\text{PO}_4)_3$ (36-39), $\text{Li}_9\text{V}_3(\text{P}_2\text{O}_7)_3(\text{PO}_4)_2$ (40), and V_2O_5 (41-43) cathode materials during lithiation. Thus, the SVOP cathode material reported here is unique because the initial preference of Ag⁺ or V⁵⁺ reduction can be controlled by discharge rate. After the first 0.2 electrons DOD the EIS data indicate that at both C/400 and C/170 there is a concomitant reduction of Ag^+ to Ag^0 and V^{n+} to $V^{(n-1)+}$.

In conjunction with the electrochemical tests and in-situ EDXRD it appears that a C/170 rate incites V⁵⁺ reduction preferentially to Ag⁺ reduction because it is a more facile reduction mechanism, resulting in cathode crystal deformation and increasing cathode resistance during the first 0.2 electrons DOD. The initial reaction for SVOP discharged at the C/170 rate is displayed in Equation (1) which is then followed by reactions written in Equation (2a) and (2b). Discharge at C/400 displayed a more balanced reduction of V⁵⁺ and Ag⁺ during the first 0.2 electrons DOD with formation of a complete conductive Ag⁰ network at earlier DOD (Figure 4). After 0.2 electrons DOD both rates decrease in charge transfer resistance and increase in Ag⁰ diffraction intensity. At C/170, the reduction mechanism is shown in two steps as no silver formation is observed below 0.2 electrons, but from 0.2 – 0.5 electrons, competition between silver reduction and vanadium reduction is observed up to 0.5 electrons. The concomitant reduction reactions at the C/400 rate are revealed in Equation (3a) and (3b).

$$\frac{\text{C}/170 \text{ Discharge (first 0.2 electrons DOD)}}{\text{Ag}_{0.50}V_{0.50}^{5+}V_{0.50}^{4+}\text{OPO}_4} \xrightarrow{\text{xLi (x \leq 0.20)}} \text{Li}_x \text{Ag}_{0.50}V_{0.50-x}^{5+}V_{0.50+x}^{4+x}\text{OPO}_4}$$
[1]

C/170 Discharge Concomitant Reactions (following 0.8 electrons DOD)

$$\text{Li}_{x} \text{Ag}_{0.50} V_{0.50-x}^{5+} V_{0.50+x}^{4+x} \text{OPO}_{4} \xrightarrow{\text{yLI } (y \leq 0.50)} \text{Li}_{x+y} \text{Ag}_{0.50-y} V_{0.50-x}^{5+} V_{0.50+x}^{4+x} \text{OPO}_{4} + y \text{Ag}^{0}$$
 [2a]
$$\text{Li}_{x} \text{Ag}_{0.50} V_{0.50-x}^{5+} V_{0.50+x}^{4+x} \text{OPO}_{4} \xrightarrow{\text{wLI } (w \leq 0.30)} \text{Li}_{x+w} \text{Ag}_{0.50} V_{0.50-x-w}^{5+} V_{0.50+x+w}^{4+x} \text{OPO}_{4}$$
 [2b]

C/400 Discharge Concomitant Reactions (up to 1 electron DOD)

$$Ag_{0.50}V_{0.50}^{5+}V_{0.50}^{4+}OPO_{4} \xrightarrow{\text{xLi }(x \le 0.50)} Li_{x}Ag_{0.50}V_{0.50-x}^{5+}V_{0.50+x}^{4+x}OPO_{4}$$

$$Ag_{0.50}V_{0.50}^{5+}V_{0.50}^{4+}OPO_{4} \xrightarrow{\text{yLI }(y \le 0.50)} Li_{y}Ag_{0.50-y}V_{0.50}^{5+}V_{0.50}^{4+}OPO_{4} + yAg^{0}$$
[3a]

$$Ag_{0.50}V_{0.50}^{5+}V_{0.50}^{4+}OPO_4 \xrightarrow{\text{yLf (y \le 0.50)}} Li_yAg_{0.50-y}V_{0.50}^{5+}V_{0.50}^{4+}OPO_4 + yAg^0$$
 [3b]

Spatial Distribution of Reduction Products

In addition to analyzing the rate dependent reduction mechanism through crystal changes in-situ EDXRD also provides unique insight into the spatial distribution of the reduction process. The influence of ionic and electronic conductivity limitations are clearly observed from the spatial distribution of reduced active material which allows for optimization of electrode design and full utilization of active material.

Figure 4 depicts the development of the (111) reflection from Ag⁰ formation inside the SVOP cathode during discharge. From these plots it is clear that by 0.6 electron equivalents there (Figure 4e) is a significant amount of metallic silver formed but the distribution of Ag⁰ is not the same for the two discharge rates. At C/170 metallic silver is mostly present on the side of the cathode facing the lithium anode with significantly less silver in the center of the cathode or current collector side. Discharge at C/400 resulted in more even distribution of Ag⁰ throughout the thickness of the cathode. The diminishing (006) SVOP reflection during discharge also showed a heterogeneous distribution for the faster rate and homogeneous distribution at the slower rate. At C/170 the (006) reflection quickly decreased in intensity near the current collector while remaining present on the lithium-facing side. In contrast, at C/400 the (006) reflection decreased in intensity relatively evenly through the cathode as discharge progressed. Initial reduction of SVOP behaves similarly to other transition metal phosphate active materials like LiFePO₄ constrained by their inherent poor electrical conductivity. A few studies imaged the reduction process of LiFePO₄ electrodes with similarities to the initial discharge of SVOP (21, 44-49). A recent study of the spatial lithiation and delithiation of LiFePO₄ using in-operando transmission hard x-ray microscopy showed that a faster rate provokes heterogeneous particle deliathion or lithiation while a sample charged or discharged 50 times slower exhibited more homogeneous distribution of particle delithiation or lithiation (44). At a faster rate some particles fully delithiate before other particles even begin to delithiate and at a slower rate most particles simultaneously delithiate.

A decrease in intensity of the (006) SVOP peak associated with vanadium reduction was noted close to the current collector at C/170 (Figure 5), while the Ag⁰ (111) peak formed on the surface facing the anode (Figure 4). This suggests a dual reaction front but can be rationalized with limitations of ionic and electronic conductivity. Cells discharged at C/170 require a greater flux of electron transfer which is impeded by the initially nonconductive SVOP particles. Early V⁵⁺ reduction occurs near the current collector because there is an incomplete conductive network of graphite and electrically connected SVOP particles near the current collector reduced first.

Since there is a low loading of graphite (5 wt% or ~7 vol%) there is insufficient graphite content to form a complete graphite network which results in a high portion of electrically connected SVOP particles closer to the current collector and some electrically

isolated particles near the anode-facing side of the cathode. The graphite particles used in this study can be approximated as thin oblate spheroids or plates with an aspect ratio of 1:10 relative to length of symmetry axis to length of the axis perpendicular to the symmetry axis. The percolation threshold for this geometry is about 10.6 vol% graphite in order to form a complete percolation network (50). This means that all graphite particles in the pellet are not necessarily connected since graphite occupies a smaller volume than the percolation network threshold. These findings agree with a study which used transmission x-ray microscopy to spatially resolve the location of lithiation of LiFePO₄ electrodes with different carbon content (46). An incomplete graphite percolation network assists in rationalizing the decreasing SVOP peak intensity at 0.2 electrons DOD for the C/170 rate since there are electrically insulated SVOP particles on the anode-facing part of the cathode which are not lithiated and retain their SVOP structure while particles closer to the current collector become lithiated. process is not evident in the EDXRD scans for the C/400 rate as they retain SVOP crystallinity through all points in the cathode through 0.4 electron DOD (Figure 5).

For the C/170 rate Ag⁰ deposits preferentially on the anode facing side because slow electron transfer is no longer an issue once conductive Ag⁰ is formed. Based on EIS measurements, the cathode conductivity increases between 0.1 and 0.4 electrons of discharge. In Figure 4 the cells discharged at C/170 show a much greater Ag⁰ peak intensity near the lithium-facing side of the cathode indicating that reduction no longer favors particles near the current collector. Silver reduction preferentially occurred at the lithium-facing surface because they are the most accessible for Li⁺ insertion. The initial reduction of V⁵⁺ is limited by electron transport, but the reduction of Ag⁺ is limited by Li⁺ ion diffusion. An ex-situ micro x-ray diffraction study of the cross-section of a LiFePO₄ cathode showed that at faster rates discharge is limited by ion diffusion and the surface facing the Li anode will reduce first (45). In a similar study x-ray absorption spectroscopy was used to map the reaction distribution and relaxation of LiCoO₂ and LiFePO₄ showing reduction beginning near the current collector and propagating outward through the cathode (49). Once Ag⁰ was deposited on the cathode surface, a conductive network of Ag⁰ contacted nondischarged SVOP particles and provided an electron pathway for their reduction. However, each position in the cathode did not produce the same amount of Ag⁰ since there is a noticeable difference in peak intensity between the current collector and Li-facing sides of the cell discharged at C/170.

A similar Ag⁺ reduction mechanism can be applied to the cells discharged at C/400. The slower discharged cells show a more uniform Ag⁰ peak intensity throughout the cathode with a slight decrease in intensity near the current collector. There could be a less exaggerated preference for Ag⁺ reduction of particles near the anode-facing surface because a slower discharge rate can accommodate slow Li⁺ diffusion into the pellet which permits a more even distribution of particle reduction and less isolated inactive particles. These isolated regions contribute to the capacity difference between the faster and slower discharged cells. During the early stages of reduction when small amounts of silver are present, differences in silver formation due to rate dependence of the reduction mechanisms at the C/170 and C/400 rates result in significant differences in observed cell resistance. However, once sufficient silver is present to form a highly interconnected conductive network within the electrode (i.e. 1.0 electron equivalent), the locational differences have less impact on the cell impedance.

The proposed discharge mechanism of SVOP pellets with 5 wt% graphite is illustrated in Figure 8. At C/170 discharge rate vanadium reduction begins and continues through 0.2 electrons DOD near the current collector and the connected graphite network.

At C/170 silver reduction begins at the anode-facing surface of the pellet and propagates through the cathode. At the C/170 discharge rate a zone in the interior of the pellet with isolated particles that were not reduced was observed. At C/400 silver reduction occurs earlier and more evenly through the cathode creating a more complete conductive matrix throughout the cathode thickness. Thus, the C/400 rate developed a more homogenous silver network and particle reduction. A homogeneous distribution of silver and SVOP reduction results in a fuller utilization of active material, formation of a complete conductive network at earlier DOD and greater achieved discharge capacity whereas a heterogeneous silver network results in unused active material blocked from ionic or electronic transport.

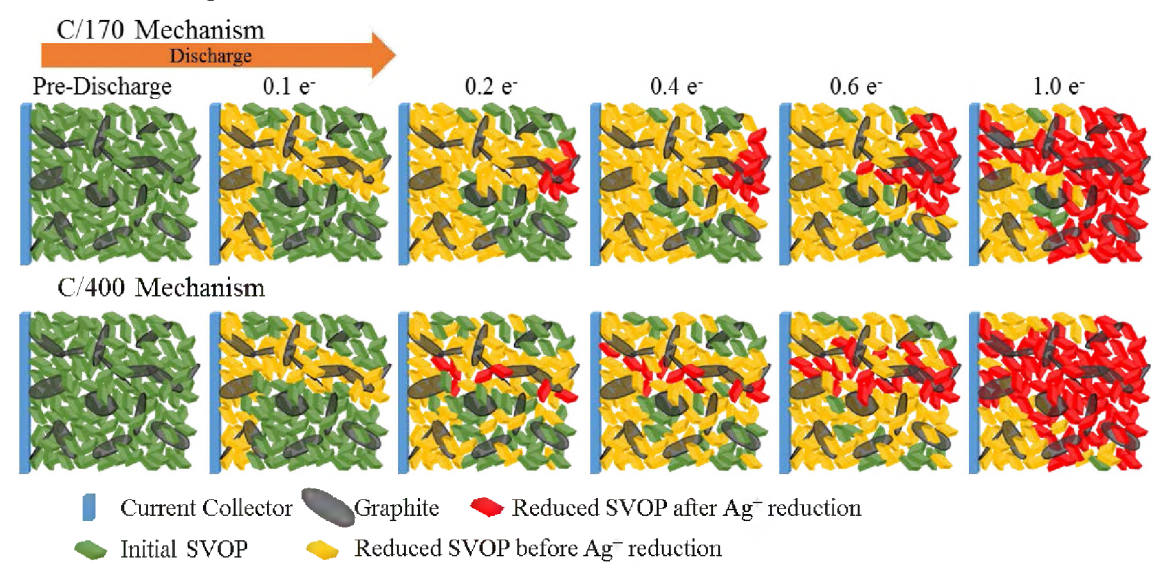


Figure 8. Illustrated reduction mechanism of SVOP pellets with 5 wt% graphite based on *in-situ* EDXRD results. SVOP is initially reduced near electrically conducting components followed by Ag⁰ formation on the anode-facing surface with a propagating Ag⁰ network.

The findings presented here illuminate the roles of ionic and electronic transport within a nonconductive transition metal phosphate cathode. *In-situ* EDXRD was used to investigate nonconductive SVOP material which undergoes reduction to form an electronically conductive Ag⁰ matrix. This unique material allows for the study of a multi-mechanism reaction involving two metal centers and either reduction displacement or lithium ion insertion. These results have significant implications to other nonconductive transition metal phosphate or oxide compounds and optimal electrode design.

Conclusion

This report applied *in-situ* EDXRD using synchrotron radiation to track the reduction mechanism of Ag_{0.50}VOPO₄·1.8H₂O inside an intact Li battery. *In-situ* EDXRD allowed for analysis of the cathode crystal structure changes during battery. At a C/170 discharge rate V⁵⁺ reduction was preferred over reduction-displacement of Ag⁺ while at a rate of C/400 the formation of conductive Ag⁰ took place at an earlier depth of discharge. Discharge rate greatly influenced the location of the reduction reaction within the cathode. Cells discharged at a faster rate provoked a non-uniform reduction process

resulting in an uneven distribution of reduced Ag^0 and loss of crystallinity in parts of the cathode near the current collector. A slower discharge rate resulted in a more homogeneous distribution of Ag^0 while the parent material retained its original crystal structure at a deeper depth of discharge indicating a fuller utilization of the active material. This study provided insight regarding the roles of electron and ionic conductivity in cathode reduction and how they affect performance at different rates of discharge.

Acknowledgments

The authors acknowledge the Center for Mesoscale Transport Properties, an Energy Frontier Research Center supported by the U.S. Department of Energy, Office of Science, Basic Energy Sciences, under award #DE-SC0012673 for financial support. This research used resources of the Advanced Photon Source, a U.S. Department of Energy (DOE) Office of Science User Facility operated for the DOE Office of Science by Argonne National Laboratory under Contract No. DE-AC02-06CH11357. Use of APS Beamline 6-BM is partially supported by the National Synchrotron Light Source II, Brookhaven National Laboratory, under DOE Contract No. DE-SC0012704. MMH acknowledges that this material is based upon work supported by the National Science Foundation Graduate Research Fellowship Program under Grant No. 1109408.

References

- 1. S. Deng, H. Wang, H. Liu, J. Liu and H. Yan, *Nano-Micro Letters*, **6**, 209 (2014).
- 2. R. Malik, A. Abdellahi and G. Ceder, *Journal of the Electrochemical Society*, **160**, A3179 (2013).
- 3. J. Wang and X. Sun, Energy & Environmental Science, 8, 1110 (2015).
- 4. D. C. Bock, A. C. Marschilok, K. J. Takeuchi and E. S. Takeuchi, *Journal of Power Sources*, **231**, 219 (2013).
- 5. D. C. Bock, K. J. Takeuchi, A. C. Marschilok and E. S. Takeuchi, *Physical Chemistry Chemical Physics*, 17, 2034 (2015).
- 6. D. C. Bock, R. V. Tappero, K. J. Takeuchi, A. C. Marschilok and E. S. Takeuchi, *ACS Applied Materials & Interfaces*, 7, 5429 (2015).
- 7. Y. J. Kim, C.-Y. Lee, A. C. Marschilok, K. J. Takeuchi and E. S. Takeuchi, *Journal of Power Sources*, **196**, 3325 (2011).
- 8. Y. J. Kim, K. J. Takeuchi, A. C. Marschilok and E. S. Takeuchi, *Journal of the Electrochemical Society*, **160**, A2207 (2013).
- 9. K. Kirshenbaum, D. C. Bock, C.-Y. Lee, Z. Zhong, K. J. Takeuchi, A. C. Marschilok and E. S. Takeuchi, *Science (Washington, DC, United States)*, **347**, 149 (2015).
- 10. K. C. Kirshenbaum, M. C. Menard, Y. J. Kim, A. C. Marschilok, K. J. Takeuchi and E. S. Takeuchi, *Journal of the Electrochemical Society*, **162**, A1537 (2015).
- 11. A. C. Marschilok, K. J. Takeuchi and E. S. Takeuchi, *Electrochemical and Solid-State Letters*, **12**, A5 (2008).
- 12. A. C. Marschilok, Y. J. Kim, K. J. Takeuchi and E. S. Takeuchi, *Journal of the Electrochemical Society*, **159**, A1690 (2012).
- 13. E. S. Takeuchi, A. C. Marschilok, K. J. Takeuchi, A. Ignatov, Z. Zhong and M. Croft, *Energy & Environmental Science*, **6**, 1465 (2013).

- 14. E. S. Takeuchi, A. C. Marschilok, K. Tanzil, E. S. Kozarsky, S. Zhu and K. J. Takeuchi, *Chemistry of Materials*, **21**, 4934 (2009).
- 15. A. C. Marschilok, E. S. Kozarsky, K. Tanzil, S. Zhu, K. J. Takeuchi and E. S. Takeuchi, *Journal of Power Sources*, **195**, 6839 (2010).
- 16. B. C. Giessen and G. E. Gordon, *Science*, **159**, 973 (1968).
- 17. J. Rijssenbeek, Y. Gao, Z. Zhong, M. Croft, N. Jisrawi, A. Ignatov and T. Tsakalakos, *Journal of Power Sources*, **196**, 2332 (2011).
- 18. G. Liang, M. C. Croft and Z. Zhong, *Journal of the Electrochemical Society*, **160**, A1299 (2013).
- 19. W. A. Paxton, E. K. Akdogan, I. Savkliyildiz, A. U. Choksi, S. X. Silver, T. Tsakalakos and Z. Zhong, *Journal of Materials Research*, **30**, 417 (2015).
- 20. W. A. Paxton, Z. Zhong and T. Tsakalakos, *Journal of Power Sources*, **275**, 429 (2015).
- 21. F. C. Strobridge, B. Orvananos, M. Croft, H.-C. Yu, R. Robert, H. Liu, Z. Zhong, T. Connolley, M. Drakopoulos, K. Thornton and C. P. Grey, *Chemistry of Materials*, **27**, 2374 (2015).
- 22. S. Bhadra, B. J. Hertzberg, A. G. Hsieh, M. Croft, J. W. Gallaway, B. J. Van Tassell, M. Chamoun, C. Erdonmez, Z. Zhong, T. Sholklapper and D. A. Steingart, *Journal of Materials Chemistry A: Materials for Energy and Sustainability*, **3**, 9395 (2015).
- 23. J. W. Gallaway, C. K. Erdonmez, Z. Zhong, M. Croft, L. A. Sviridov, T. Z. Sholklapper, D. E. Turney, S. Banerjee and D. A. Steingart, *Journal of Materials Chemistry A: Materials for Energy and Sustainability*, **2**, 2757 (2014).
- 24. J. W. Gallaway, M. Menard, B. Hertzberg, Z. Zhong, M. Croft, L. A. Sviridov, D. E. Turney, S. Banerjee, D. A. Steingart and C. K. Erdonmez, *Journal of the Electrochemical Society*, **162**, A162 (2015).
- 25. H. Murayama, K. Kitada, K. Fukuda, A. Mitsui, K. Ohara, H. Arai, Y. Uchimoto, Z. Ogumi and E. Matsubara, *The Journal of Physical Chemistry C*, **118**, 20750 (2014).
- 26. K. Kitada, H. Murayama, K. Fukuda, H. Arai, Y. Uchimoto, Z. Ogumi and E. Matsubara, *Journal of Power Sources*, **301**, 11 (2016).
- 27. K. J. Takeuchi, S. Z. Yau, A. Subramanian, A. C. Marschilok and E. S. Takeuchi, *Journal of the Electrochemical Society*, **160**, A3090 (2013).
- 28. J. L. Durham, K. Kirshenbaum, E. S. Takeuchi, A. C. Marschilok and K. J. Takeuchi, *Chemical Communications (Cambridge, United Kingdom)*, **51**, 5120 (2015).
- 29. K. C. Kirshenbaum, D. C. Bock, Z. Zhong, A. C. Marschilok, K. J. Takeuchi and E. S. Takeuchi, *Physical Chemistry Chemical Physics*, **16**, 9138 (2014).
- 30. K. C. Kirshenbaum, D. C. Bock, Z. Zhong, A. C. Marschilok, K. J. Takeuchi and E. S. Takeuchi, *Journal of Materials Chemistry A: Materials for Energy and Sustainability*, **3**, 18027 (2015).
- 31. P. Ayyappan, A. Ramanan and C. C. Torardi, *Inorganic Chemistry*, **37**, 3628 (1998).
- 32. Y. J. Kim, A. C. Marschilok, K. J. Takeuchi and E. S. Takeuchi, *Journal of Power Sources*, **196**, 6781 (2011).
- 33. W. M. Haynes, *Handbook of Chemistry and Physics*, Chemical Rubber Company (2012).
- 34. C. J. Patridge, C. Jaye, T. A. Abtew, B. Ravel, D. A. Fischer, A. C. Marschilok, P. Zhang, K. J. Takeuchi, E. S. Takeuchi and S. Banerjee, *Journal of Physical Chemistry C*, **115**, 14437 (2011).

- 35. Y. Song, P. Y. Zavalij and M. S. Whittingham, *Journal of the Electrochemical Society*, **152**, A721 (2005).
- 36. X. H. Rui, N. Ding, J. Liu, C. Li and C. H. Chen, *Electrochimica Acta*, **55**, 2384 (2010).
- 37. X. H. Rui, N. Yesibolati, S. R. Li, C. C. Yuan and C. H. Chen, *Solid State Ionics*, **187**, 58 (2011).
- 38. J. Wang, H. Zhang, S. Zheng, M. Hojamberdiev, B. Ren, Y. Xu and C. Shao, *Materials Chemistry and Physics*, **148**, 569 (2014).
- 39. L. Wang, J. Xu, C. Wang, X. Cui, J. Li and Y.-N. Zhou, *RSC Advances*, **5**, 71684 (2015).
- 40. Q. Kuang, Y. Zhao and J. Xu, *Journal of Physical Chemistry C*, **115**, 8422 (2011).
- 41. H. M. Song, D. Y. Yoo, S. K. Hong, J. S. Kim, W. I. Cho and S. I. Mho, *Electroanalysis*, **23**, 2094 (2011).
- 42. A. Sakunthala, M. V. Reddy, S. Selvasekarapandian, B. V. R. Chowdari and P. C. Selvin, *Energy & Environmental Science*, **4**, 1712 (2011).
- 43. L. Shao, K. Wu, X. Lin, M. Shui, R. Ma, D. Wang, N. Long, Y. Ren and J. Shu, *Ceramics International*, **40**, 6115 (2014).
- 44. J. Wang, Y.-c. K. Chen-Wiegart and J. Wang, *Nature Communications*, **5**, 4570 (2014).
- 45. J. Liu, M. Kunz, K. Chen, N. Tamura and T. J. Richardson, *Journal of Physical Chemistry Letters*, **1**, 2120 (2010).
- 46. J. Nelson Weker, Y. Li, R. Shanmugam, W. Lai and W. C. Chueh, *ChemElectroChem*, **2**, 1576 (2015).
- 47. W. C. Chueh, F. El Gabaly, J. D. Sugar, N. C. Bartelt, A. H. McDaniel, K. R. Fenton, K. R. Zavadil, T. Tyliszczak, W. Lai and K. F. McCarty, *Nano Letters*, **13**, 866 (2013).
- 48. D. Robert, T. Douillard, A. Boulineau, G. Brunetti, P. Nowakowski, D. Venet, P. Bayle-Guillemaud and C. Cayron, *ACS Nano*, 7, 10887 (2013).
- 49. H. Tanida, H. Yamashige, Y. Orikasa, Y. Gogyo, H. Arai, Y. Uchimoto and Z. Ogumi, *Journal of Physical Chemistry C*, **120**, 4739 (2016).
- 50. E. J. Garboczi, K. A. Snyder, J. F. Douglas and M. F. Thorpe, *Physical Review E: Statistical Physics, Plasmas, Fluids, and Related Interdisciplinary Topics*, **52**, 819 (1995).